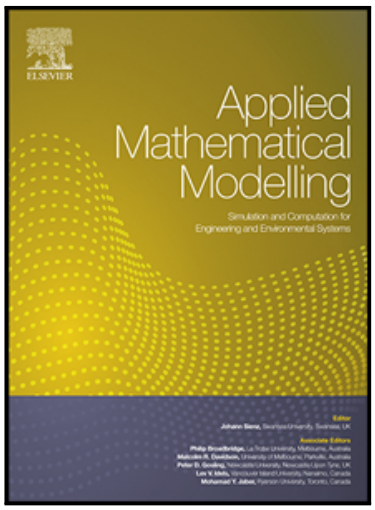

Towards a better understanding of wall-driven square cavity flows using the Lattice Boltzmann method

Bo AN , F. Mellibovsky , J.M. Bergadà , W.M. Sang

PII: S0307-904X(20)30065-2
DOI: https://doi.org/10.1016/j.apm.2020.01.057
Reference: APM 13270

To appear in: *Applied Mathematical Modelling*

Received date: 22 August 2019
Revised date: 15 January 2020
Accepted date: 22 January 2020

Please cite this article as: Bo AN , F. Mellibovsky , J.M. Bergadà , W.M. Sang , Towards a better understanding of wall-driven square cavity flows using the Lattice Boltzmann method, *Applied Mathematical Modelling* (2020), doi: https://doi.org/10.1016/j.apm.2020.01.057

Highlights

- Hopf bifurcation appears between (8000, 8050), (9500, 9550) and (10100, 10200) respectively.
- Neimark-Sacker bifurcation appears between (13500, 14000), (12250, 13000) and (11000, 11100) respectively.
- Chaotic property appears between *Re* (16500, 17000) for all three cases.
- Flow symmetry disappear as soon as flow periodicity appears.
- Energy cascade and the frequency associated to each vortical structure are analyzed and discussed.

Corresponding author. Tel. 1: +34 691173315; Tel. 2: +34 937398771.
E-mail address: bo_alan_an@163.com (BO AN)

Towards a better understanding of wall-driven square cavity flows using the Lattice Boltzmann method

Bo AN[a], F. Mellibovsky[b], J.M. Bergadà[a] and W.M. Sang[c]

[a]*Department of Fluid Mechanics, Universitat Politécnica de Catalunya, 08034, Barcelona, Spain*
[b]*Department of Physics, Aerospace Engineering Division, Universitat Politécnica de Catalunya, 08034, Barcelona, Spain*
[c]*School of Aeronautics, Northwestern Polytechnical University, Xi'an, China*

Abstract

Wall-driven flow in square cavities has been studied extensively, yet it appears some main flow characteristics have not been fully investigated. Previous research on the classic lid-driven cavity (*S1*) flow has produced the critical Reynolds numbers separating the laminar steady and unsteady flows. Wall-driven cavities with two opposing walls moving at the same speed and the same (*S2p*) or opposite (*S2a*) directions have seldom been studied in the literature and no critical Reynolds numbers characterizing transitional flows have ever been investigated. After validating the LBM code for the three configurations studied, extensive numerical simulations have been undertaken to provide approximate ranges for the critical Hopf and Neimark-Sacker bifurcations for the classic and two two-sided cavity configurations. The threshold for transition to chaotic motion is also reported. The symmetries of the solutions are monitored across the various bifurcations for the two-sided wall driven cavities. The mirror-symmetry of the base solution for case *S2p* is lost at the Hopf bifurcation. The exact same scenario occurs with the pi-rotational symmetry of the base state for case *S2a*.

Keywords: lattice Boltzmann method, wall driven cavities, transitional flow, symmetry property

1. Introduction

As a relatively new and promising numerical tool, the lattice Boltzmann method was originated and developed from the lattice gas automata (LGA) [1-3]. Based on the work performed by previous scholars [4-6], the lattice Boltzmann method gradually improved to be a trustable numerical methodology. It turned out that the lattice Boltzmann method is numerically capable of solving many mathematical and physical problems, including all sorts of partial differential equations [7-10], applications such as acoustic wave phenomena [11-12], multi-phase flows [13-14], combustion [15-16], fluid mechanics [17-18], and many others.

The present manuscript, focuses on the study of three wall-driven cavity configurations with various driving conditions: the classic lid-driven cavity flow (*S1*), and the cavity flow driven by the tangential motion of two opposing walls with equal speed in parallel (*S2p*) and anti-parallel directions (*S2a*).

The present study starts with the in-house code validation, followed by the resolution study and ends with the new results and discussions on the transitional flow inside the cavity with the three different driving conditions (*S1*, *S2a* and *S2p*). In order to validate the numerical models presented, the results from references [19] and [20] are used to make the comparison with the simulated results of case *S1*. Ghia et al [19] presented a vorticity-stream-function based method to solve the 2D incompressible Navier-Stokes equations. Schreiber et al [20] provided a numerical method combining a linear solver, a Newtown-like non-linear solver and a continuation procedure, covering a range of Reynolds numbers comprised between 1 to 10000. When considering cases *S2p* and *S2a*, the computational results by Arun et al [21] have been used to compare with our present results.

Regarding some of the latest research on the square cavity, Hegele et al [22] presented a study about the flow inside a 3D square cavity by using the lattice Boltzmann method, where they implemented a special boundary condition to stabilize the turbulence model at Reynolds numbers up to 5×10^4. Samantaray and Das [23] introduced a numerical study on incompressible turbulent flow inside a 3D lid-driven cavity with a series of span-to-length and depth-to-length aspect ratios. In their work, they employed the dynamic Smagorinsky model to simulate the turbulent flow at Reynolds number 11800.

Despite the considerable amount of work done on the classic lid-driven cavity flow, little effort has been made in understanding the flow inside two-sided wall driven cavities. In fact, no previous systematic study of the flow in any of these cavities has been found in the literature. This is the reason why the authors decided to undertake a thorough systematic study of the flow properties in lid- and wall-driven cavities, including Hopf and Neimark-Sacker bifurcations, the onset of chaos, the symmetry properties and the energy cascade, which served to link the different vortical structures with the corresponding frequencies and energy associated.

Nomenclature (all parameters are non-dimensional)

$\vec{a}$	Acceleration of molecules
c_s	Sound speed
c	Lattice velocity
D	Space dimension
d_D	Particle diameter
$\vec{e}_\alpha$	Unit velocities vector along discrete directions
E	Macroscopic quantity, internal energy
$\vec{g}$	The vertical component of velocity vector difference
$f(\vec{r},\vec{\xi},t)$	Distribution function
$f^{eq}(\vec{r},\vec{\xi})$	Equilibrium distribution function
f_α	Discrete distribution functions on α directions
F_α	Discrete distribution functions on α directions after collision
$f_\alpha(\vec{r}+\vec{e}_\alpha\Delta t,t+\Delta t)$	Discrete –post collision distribution functions vector
$f_\alpha(\vec{r},t)$	Discrete –pre collision distribution functions vector
$\vec{f}_\alpha^{eq}$	Nine-ordered vector of discrete equilibrium distribution functions
$\vec{f}_\alpha'$	Discrete distribution functions vector after collision
f_α^{neq}	The non-equilibrium state of distribution functions
L	Non-dimensional characteristic length
Re	Reynolds number

R	Gas constant
$\vec{r}$	Spatial position vector
t	Time
T	Temperature
$\vec{u}$	Macroscopic quantity, velocity
U	Initial velocity of the flow field
$\bar{U}$	Steady solution of the velocity time series on x direction
$\bar{V}$	Steady solution of the velocity time series on y direction
U_{lid}	Non-dimensional wall driven velocity
u_x	Horizontal component of velocity
u_x^*	Unified non-dimensional horizontal component of velocity
u_y	Vertical component of velocity
u_y^*	Unified non-dimensional vertical component of velocity
u'	Perturbation of velocity on x direction
v'	Perturbation of velocity on y direction
α	Discrete directions (from 0 to 8 in the present LBGK *D2Q9* model)
Δx	Grid spacing
Δt	Time step
ν	Kinematic viscosity
ρ	Macroscopic quantity, density
ρ_0	Initial density
τ	Single relaxation time term
ϕ_A	Mirror symmetry parameter
ϕ_B	Pi-rotational symmetry parameter
Ω_f	Collision operator
Ω_f^α	Discrete collision operator on α directions
$d\Theta$	Integral infinitesimal of angle
ω_α	Weight Coefficients

$\vec{\xi}$	Velocity vector of molecules

2. Mathematical background

2.1. Original lattice Boltzmann equations

Equation (1) presents the continuous Boltzmann equation. All parameters appearing in this equation, as well as in all the rest of the equations are non-dimensional.

$$\frac{\partial f(\vec{r},\vec{\xi},t)}{\partial t}+\vec{\xi}\cdot\frac{\partial f(\vec{r},\vec{\xi},t)}{\partial \vec{r}}+\vec{a}\cdot\frac{\partial f(\vec{r},\vec{\xi},t)}{\partial \vec{\xi}}=\iint(\mathrm{F_1F_2}-f_1f_2)d_D^2|\vec{g}|\cos\theta d\Theta d\vec{\xi}_1 \tag{1}$$

The term $f(\vec{r},\vec{\xi},t)$ represents the distribution function, $\vec{r}$ stands for the spatial position vector, t indicates the non-dimensional time, $\vec{\xi}$ defines the velocity vector, $\vec{a}$ denotes the particle acceleration, d_D characterizes the particle diameter, $\mathrm{F_1}$,$\mathrm{F_2}$ and f_1, f_2 are the post- and pre- collision distribution functions of two fluid particles, $\vec{g}$ is the vertical component of $\vec{\xi}_1-\vec{\xi}_2$ and $d\Theta$ is the angle differential. The left hand side, represents the streaming term, while the right hand side, characterizes the collision term, which is an integral-differential term in essence. Following Bhatnagar et al [24], the right hand side of equation (1) can be simplified through the *BGK* approximation, as shown in equation (2), where the collision term has been replaced by a simple collision operator Ω_f. As a result, the Boltzmann-*BGK* equation reads

$$\frac{\partial f(\vec{r},\vec{\xi},t)}{\partial t}+\vec{\xi}\cdot\frac{\partial f(\vec{r},\vec{\xi},t)}{\partial \vec{r}}+\vec{a}\cdot\frac{\partial f(\vec{r},\vec{\xi},t)}{\partial \vec{\xi}}=\Omega_f=\frac{1}{\tau}\left[f^{eq}(\vec{r},\vec{\xi})-f(\vec{r},\vec{\xi},t)\right] \tag{2}$$

The parameter τ represents the singular relaxation time and $f^{eq}(\vec{r},\vec{\xi})$ is the equilibrium distribution function.

The lattice Boltzmann equation is obtained through a space-time discretization process, that results in

$$f_\alpha(\vec{r}+\vec{e}_\alpha\Delta t,t+\Delta t)-f_\alpha(\vec{r},t)=\Omega_f^\alpha=\frac{1}{\tau}\left[f_\alpha^{eq}(\vec{r},\vec{\xi})-f_\alpha(\vec{r},\vec{\xi},t)\right] \tag{3}$$

The index α represents each of the possible directions of discrete velocities. $f_\alpha(\vec{r}+\vec{e}_\alpha\Delta t,t+\Delta t)$ and $f_\alpha(\vec{r},t)$ are the discrete post- and pre-collision distribution functions, respectively, and Ω_f^α is the discrete collision operator in direction α. The Navier-Stokes equations can be recovered from the discrete lattice Boltzmann equation by an adequate choice of equilibrium distribution functions [17, 25, 26]. Three relevant macroscopic physical quantities, density ρ, velocity $\vec{u}$ and internal energy E, bear a simple relation with the microscopic scale physics as represented by equilibrium distribution functions [27], given by

$$\begin{cases} \rho = \sum_{\alpha} f_{\alpha} \\ \rho\vec{u} = \sum_{\alpha} \vec{e}_{\alpha} f_{\alpha} \\ \rho E = \dfrac{\rho DRT}{2} \sum_{\alpha} (\vec{e}_{\alpha} - \vec{u})^2 f_{\alpha} \end{cases} \tag{4}$$

where D denotes the number of space dimensions, R is the non-dimensional gas constant and T refers to the non-dimensional temperature.

Qian et al [17] presented an LBGK model for the Navier-Stokes equations that turned out to be a reliable model for two-dimensional simulations. The model has since become quite popular for many LBM related applications. This model is employed in the present paper for all the numerical predictions, the equilibrium distribution functions for the 9 discrete velocities (9-bit model) are determined by

$$f_{\alpha}^{eq} = \omega_{\alpha}\rho\left[1 + \frac{\vec{e}_{\alpha}\cdot\vec{u}}{{c_s}^2} + \frac{(\vec{e}_{\alpha}\cdot\vec{u})^2}{2{c_s}^4} - \frac{u^2}{2{c_s}^2}\right] \qquad \alpha = 0,1,...,8 \tag{5}$$

where ω_{α} are the weight coefficients, and c_s denotes the non-dimensional lattice sound speed. The discrete velocities of LBGK two-dimensional 9-bit model *D2Q9*, the lattice sound speed and the weight coefficients are given by

$$\vec{e} = c\begin{bmatrix} 0 & 1 & 0 & -1 & 0 & 1 & -1 & -1 & 1 \\ 0 & 0 & 1 & 0 & -1 & 1 & 1 & -1 & -1 \end{bmatrix}$$

$$c_s = \frac{c}{\sqrt{3}} \qquad \omega_{\alpha} = \begin{cases} 4/9 & \vec{e}_{\alpha}^2 = 0 \\ 1/9 & \vec{e}_{\alpha}^2 = c^2 \\ 1/36 & \vec{e}_{\alpha}^2 = 2c^2 \end{cases} \tag{6}$$

where $c = \Delta x/\Delta t = 1$ is the non-dimensional lattice velocity, and Δx and Δt represent the lattice grid non-dimensional spacing and the non-dimensional time step, respectively.

2.2. Boundary conditions

The non-equilibrium extrapolation scheme [28], is employed to prescribe the wall boundary conditions in the current study. Wall-driven cavity flow features a unique boundary condition type, corresponding to the non-slip walls. The basic idea behind this scheme is that the distribution function in each direction can be split in two separate additive parts: a non-equilibrium and an equilibrium term.

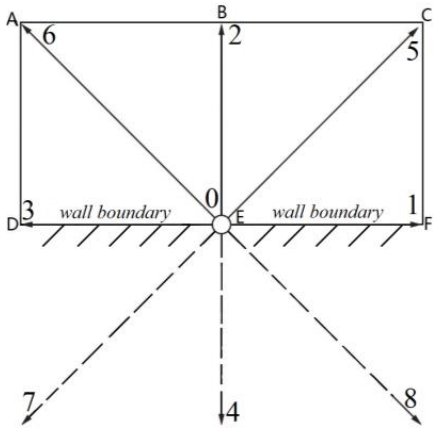

Fig. 1. Discrete velocities of lattice Boltzmann *D2Q9* model for straight wall boundaries.

As shown in Fig. 1, which represents a wall boundary condition, grid nodes ***A***, ***B*** and ***C*** are fluid domain points, while grid nodes ***D***, ***E*** and ***F*** are wall boundary points. The distribution function of each direction for the points ***E*** and ***B***, is given by equations (7) and (8).

$$f_\alpha(E,t) = f_\alpha^{eq}(E,t) + f_\alpha^{neq}(E,t) \tag{7}$$

$$f_\alpha(B,t) = f_\alpha^{eq}(B,t) + f_\alpha^{neq}(B,t) \tag{8}$$

The equilibrium part $f_\alpha^{eq}(E,t)$ is obtained from the macroscopic quantities at node ***E***, while, the non-equilibrium distribution functions at node ***E*** can be replaced by its counterpart at node ***B***.

$$f_\alpha^{neq}(E,t) \approx f_\alpha^{neq}(B,t) \tag{9}$$

Hence, the distribution functions for node ***E*** become

$$f_\alpha(E,t) = f_\alpha^{eq}(E,t) + f_\alpha(B,t) - f_\alpha^{eq}(B,t) \tag{10}$$

2.3. Code validation

All cases studied in this paper correspond to the 2D flow inside wall-driven cavities. As presented in figure 2, several wall motion configurations are considered. Case *S1* is the classic wall-driven cavity flow, where the upper lid moves horizontally in the positive *x* direction. Case *S2p* corresponds to a cavity with top and bottom walls moving in the same direction and at the same speed. Case *S2a*, instead, represents a cavity with top and bottom walls moving at equal speed but in opposite directions. For all cases, the non-dimensional wall-driving velocity is set $U_{lid} = 0.1$.

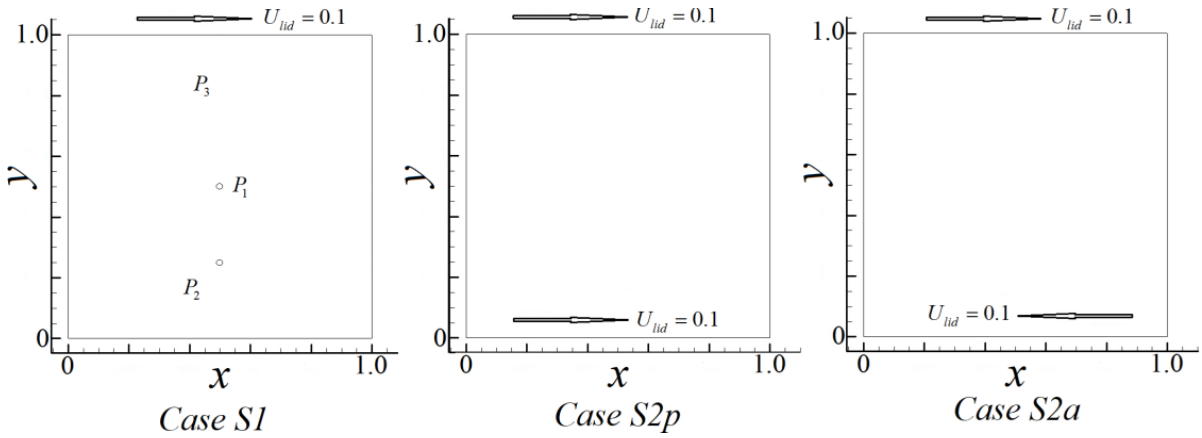

Fig. 2. Wall boundary and initial conditions of each cavity.

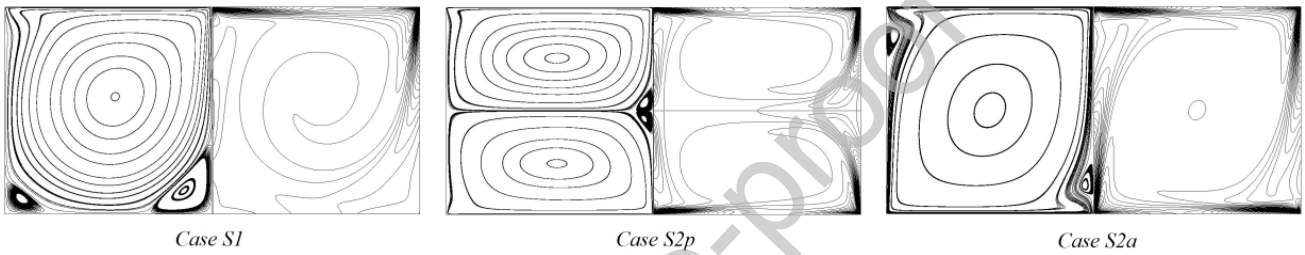

Fig. 3. Streamlines and vorticity lines of each case, the Reynolds number of cases *S1*, *S2p* and *S2a* is 1000. The resolution of each cavity is 256×256 .

In order to validate the in-house code, all three wall-driven cavity cases, *S1*, *S2p* and *S2a*, have been analysed at Reynolds 1000. Figure 3 shows the streamlines and vorticity contours of all three cases. The baseline mesh used in the figure 3 has a resolution of 256×256 grid nodes in the vertical and horizontal directions. For case *S1*, a huge central clockwise vortex covers most of the domain, while two small anti-clockwise vortices appear confined at the bottom corners. For case *S2p*, two mutually-symmetric counter-rotating vortices take the bulk of the fluid domain. Two smaller, also symmetric, counter-rotating vortices nucleate at either side of the horizontal mid-plane on the right hand side static vertical wall. For the case *S2a*, a large pi-rotational-symmetric clockwise vortex dominates the flow, while two pi-rotational-conjugate-symmetric clockwise vortices arise at the static vertical walls, close to the corners upstream from the moving walls, on the locations where the minimal pressure is to be found.

Table 1 lists the positions of all vortex cores, that are characteristic of the lid-driven cavity flow (case *S1*) at Reynolds number 1000. Our numerical results for a resolution of 256×256 are compared against published data [19, 20]. Agreement is fairly good, with a maximum relative error of about 5.5%.

Table 1. Comparison of vortex core locations of present results against published data [19 and 20], for case *S1*, at *Re*=1000, with a resolution of 256×256 .

Position	This paper	Ref.[19]	Ref.[20]
Left secondary	*X 0.081148*	*0.0859*	*0.0857*
Vortex	*Y 0.075355*	*0.0781*	*0.0714*
Right secondary	*X 0.864711*	*0.8594*	*0.8643*
Vortex	*Y 0.113206*	*0.1094*	*0.1071*

Primary	*X 0.532912*	*0.5313*	*0.5286*
Vortex	*Y 0.566457*	*0.5625*	*0.5643*

Due to fact that, one of the aims of the present paper is investigating the onset of chaos, it is relevant to validate the code at higher Reynolds numbers. The case *S1* at Reynolds number 5000, was chosen to perform this validation, figure 4 compares the results presented in references [19] and [29] with the ones obtained in the present research using a resolution of 512×512 . The agreement was very good.

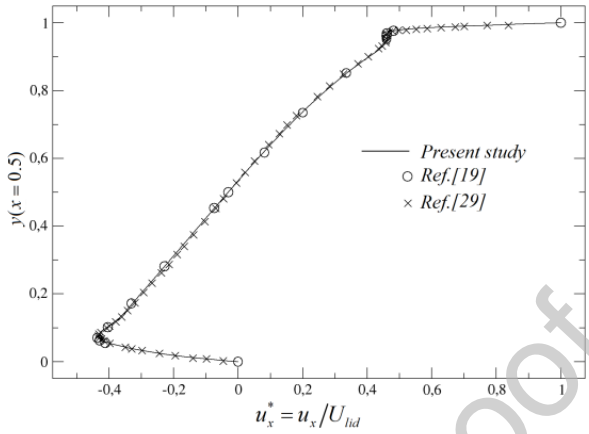

Fig. 4. Comparison of the velocity profile u_x^* between the computed results from the present paper, case *S1*, and the data from references [19 and 29], *Re* =5000, resolution 512×512 .

Table 2 lists the same vortex core positions given in table 1 but for different grid resolutions. The comparison between the results presented in table 2 and some of the previous researchers' ones, can be done when comparing tables 1 and 2. Among these cases, all parameters are kept constant except the grid resolution. It is noticed that, the computational results are becoming more accurate as the grid resolution increases. It is also observed that the computational results are acceptable and accurate enough when the grid resolution is around or above 200×200 . According to the results presented in tables 1, 2 and figure 4, it can be stated that the lattice Boltzmann method is validated for case *S1* at Reynolds numbers 1000 and 5000.

Table 2. Grid independency test of top wall driven cavity, case *S1*, the Reynolds number is 1000.

Resolution	(50,50)	(100,100)	(200,200)	(300,300)
Left secondary	*X 0.070775*	*0.07914*	*0.08146*	*0.081255*
Vortex	*Y 0.062431*	*0.07332*	*0.07518*	*0.075214*
Right secondary	*X 0.862163*	*0.86334*	*0.86443*	*0.864734*
Vortex	*Y 0.11589*	*0.11407*	*0.113*	*0.113114*
Primary	*X 0.536735*	*0.53366*	*0.5327*	*0.532948*
Vortex	*Y 0.576075*	*0.5687*	*0.56665*	*0.5666489*

In order to further check the performance of the LBM approach used, the velocity profiles along the vertical central line, at $x=0.5$, and the horizontal line, at $y=0.75$, are presented in figure 5, for cases *S2p* and *S2a*. The comparison between the numerical predictions calculated in the present paper and the data by Arun et al [21] shows excellent agreement, which reinforces the applicability of the LBM model used for the other two cavity flow configurations explored at this Reynolds number.

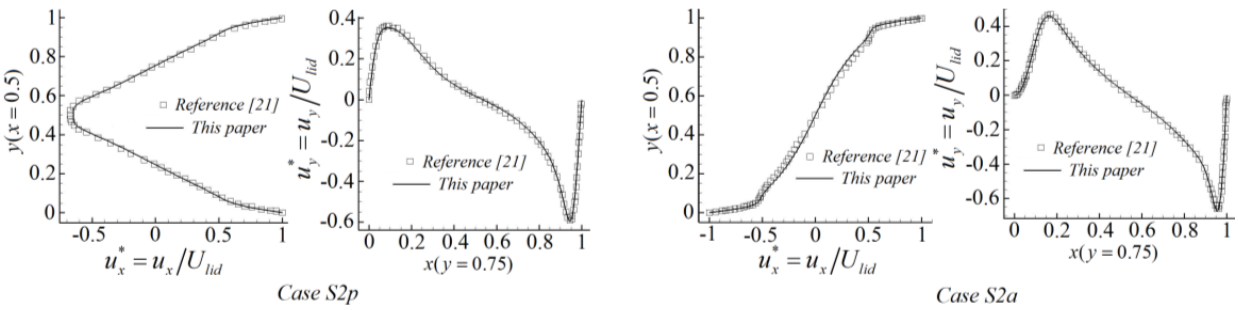

Fig. 5. Comparison of the velocity profiles between the computed results from the present paper, cases *S2p* and *S2a*, and the data from reference [21], *Re* =1000, resolution 256×256.

2.4. Resolution study

According to the related literature review study on wall-driven square cavities, it is found that Ghia et al [19] using the resolution 256×256, studied the lid-driven cavity flow with Reynolds numbers up to 10000. Schreiber et al [20] employed the resolution 180×180 to investigate the lid-driven cavity flow at Reynolds numbers ranging from 1 to 10000. Arun et al [21] carried out their study on the two-sided lid-driven cavity at Reynolds number 5000 with a resolution of 258×258. Bruneau and Jouron [30] employed the resolution 256×256 in the study of the lid-driven cavity flow at Reynolds numbers up to 5000. Huser et al [31] analyzed the lid-driven cavity flow, for Reynolds numbers up to 30000, with a resolution of 160×160. Fortin et al [32] researched the lid-driven cavity flow with a resolution of 60×60 for a Reynolds number 8000. Auteri et al [33] studied the bifurcation inside the lid-driven cavity with a resolution of 160×160, the largest Reynolds number was 10000. Peng et al [34] studied the transition in the lid-driven cavity with a resolution of 120×120 and they did a grid independence test at Reynolds number 5000, reporting a relative error of 6.8×10^{-4}. Sahin et al [35] did a high Reynolds number study on the lid-driven cavity flow, he employed a resolution of 256×256 at Reynolds numbers up to 10000. Brueau and Saad [36], introduced a series of grid independency tests, the largest Reynolds number tested was 10000 based on a resolution of 1024×1024. For a periodic solution at Re 8200, they reported identical results with both 512×512 and 1024×1024 resolutions but pushed the resolution to 2048×2048, in order to provide highly accurate results at Reynolds number 5000.

Figure 6 shows several computational results, for cases *S1*, *S2p* and *S2a* (see figure 2), when using different grid resolutions. It is observed that, for the Reynolds number evaluated, *Re*=1000, the grid resolution between 200×200 and 300×300 produces very accurate results. Notice that, in each figure, the zoomed view of the curve main discrepancy area is presented.

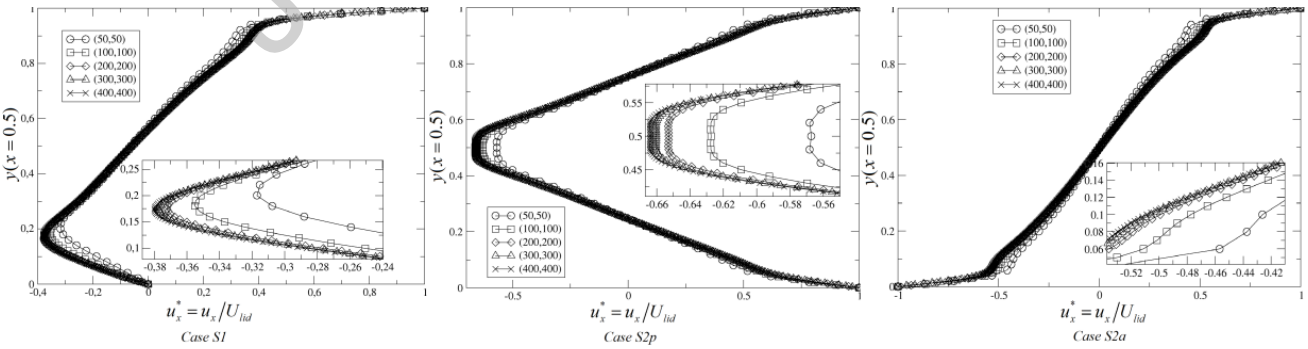

Fig. 6. Grid independence study of two sided wall-driven cavities (cases *S2p* and *S2a*) and lid-driven cavity (case *S1*) at *Re* =1000. Each figure shows the zoomed zone where the small disagreement is spotted.

Table 3 provides a further quantification of the accuracy by measuring the relative error of u_x at the cavity centre as resolution is increased for case *S1* at Re=1000. The solution with the highest resolution 512×512, which corresponds to a steady state, is taken as the base line for error estimation. The relative error is seen to drop considerably for resolutions beyond 200×200. Literature results with resolutions of 512×512 are reported as highly accurate for computing the laminar steady solution that arises for the lid-driven cavity flow at Reynolds 1000 [19-21]. Here we have shown that a resolution of 300×300 is sufficient to accurately resolve case *S1* at Reynolds number 1000 when using the lattice Boltzmann method.

Table 3. Relative error of different grid spacing over the minimum grid spacing (Δx =0.00195) at Reynolds number 1000, case *S1*.

Resolution	50,50	100,100	200,200	300,300	400,400	512,512
Relative error	*0.3912*	*0.224*	*0.007687*	*0.003638*	*0.001324*	*0.0*

Table 4. Frequencies of time series of u_x with different resolutions for case *S1* at Reynolds number 8800.

Resolution	100,100	200,200	300,300	512,512	800,800	1024,1024
Frequency	*chaotic*	*chaotic*	*steady*	*0.4295*	*0.4321*	*0.4374*

Table 5. Frequencies of time series of u_x with different resolutions for case *S2p* at Reynolds number 9900.

Resolution	100,100	200,200	300,300	512,512	800,800	1024,1024
Frequency	*steady*	*steady*	*steady*	*1.415658*	*1.423*	*1.44095*

Table 6. Frequencies of time series of u_x with different resolutions for case *S2a* at Reynolds number 11000.

Resolution	100,100	200,200	300,300	512,512	800,800	1024,1024
Frequency	*steady*	*steady*	*steady*	*1.1775*	*1.1943*	*1.2083*

In order to extend the grid independence study for transitional flows, the results obtained when using various resolutions, were evaluated for the cases *S1*, *S2p* and *S2a* at Reynolds number 8800, 9900 and 11000 respectively. Tables 4, 5 and 6 show the frequencies of periodic solutions based on different resolutions, ranging from 100×100 to 1024×1024. The results were obtained from the probe P_1 located at position $\left(x=L/2,\ y=L/2\right)$ for cases *S1* and *S2p* and the probe P_2 located at position $\left(x=L/2,\ y=L/4\right)$ for case *S2a*, see figure 2 (a). It is observed that as the Reynolds number increases, the mesh needs to be refined to obtain trustable results. Therefore, for the rest of the paper, a resolution of 1024×1024 is employed for all cases. For all the cases, the mesh used is a standard Cartesian grid.

3. Results and discussion

3.1. Transitional flow study for case S1

According to different authors, the critical Reynolds number of the transitional flow from laminar steady to laminar unsteady in case *S1* are expected to have the following values, 7500 [30, 34], 6000-8000 [29, 37, 38], 8000 [31, 32, 33, 36], 8000-8300 [11] and 8000-8051 [33, 35, 39-41]. Koseff and Street [42, 43] experimentally investigated the lid-driven cavity flow and determined the critical Reynolds number for the Hopf bifurcation was between 6000 and 8000. This conclusion was also obtained by Prasad and Koseff [37] in their experiments. Bruneau and Jouron [30], numerically investigated the Hopf bifurcation via employing

2D finite differences, obtaining a value of 7500. Huser et al [31] analyzed the lid-driven cavity, for Reynolds numbers up to 30000 with resolution 160×160 . Peng et al [34] found that the critical Reynolds number was 7500 via analyzing the velocity history, phase-space trajectories of velocity u_y versus velocity u_x , and Fourier spectra of velocity u_x . In the work performed by Bruneau and Saad [36], using as well 2D finite differences, the critical Reynolds number was estimated at 8000 by analyzing the evolution of Lyapunov exponents as Reynolds number was increased towards criticality. Via linearizing the N-S equations and obtaining a pair of eigenvalues from the Jacobian matrix, which crosses the imaginary axis, Fortin et al [32] obtained the critical Reynolds number 8000. Auteri et al [33] figured out the critical Reynolds number 8000 via using a second-order spectral projection method. In two further articles undertaken by Zhuo et al [38] and Lin et al [29], by using lattice Boltzmann method, they presented the ranges of the Hopf bifurcation, which were appearing around $[8200,8250]$ and $[8325,8350]$ respectively. In the research performed by Murdock et al [44], they reported the Hopf bifurcation happens in the Reynolds number interval 7988.2 ± 19 . Sahin and Owens [35] investigated the linear stability of the steady state using a novel implicit finite volume method, in combination with Arnoldi iteration to produce a critical Reynolds of 8031.93. An extended review of the literature on the lid-driven cavity flow Hopf bifurcation provides critical Reynolds numbers of 8018.2 ± 0.6 [33], 8026.7 [39], 8025.9 [40] or 8051 [41].

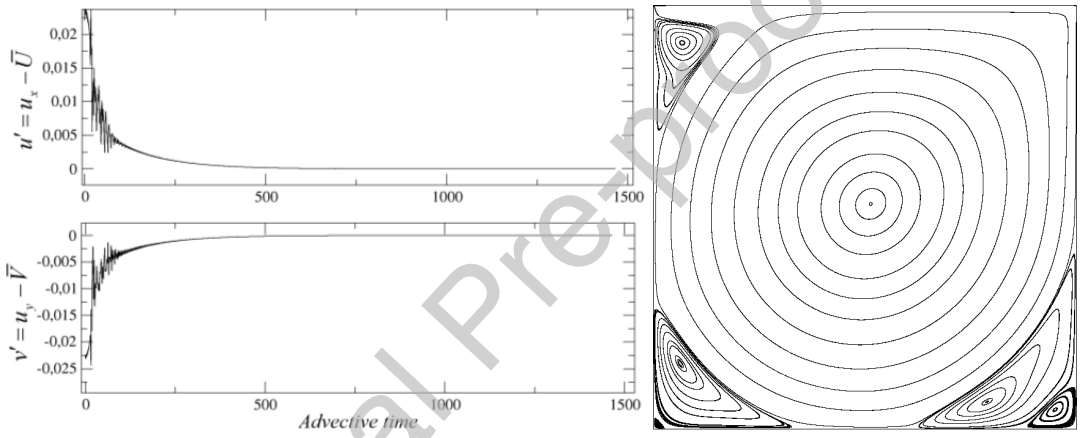

(a) (b)

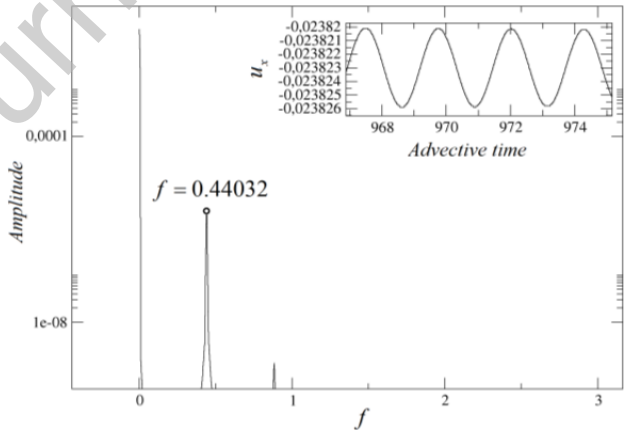

(c)

Fig. 7. (a) Perturbation of velocity history (u' and v') of the monitoring point at *Re*=8000, (b) Streamlines topology at *Re*=8000. (c) Periodic orbit at *Re*=8050.

Figure 7 (b) shows a collection of streamlines of the steady state at *Re*=8000 to illustrate its flow topology. At this value of the Reynolds number and below, time evolution drives the flow towards this well-known steady state, consisting of a large clockwise vortex that occupies the centre of the cavity that is flanked by three anti-clockwise vortices on the left wall close to the top corner and at the two bottom corners. The latter engulf a cascade of ever smaller vortices of alternate sense of rotation as the corners are approached. We have monitored the final approach towards the steady state with a probe P_1 located at the centre of the cavity.

Figure 7 (a) shows decay of the two components of the perturbation velocity at this point. Following some initial transients, the signal asymptotically approaches the constant value that characterizes the steady state. Direct time evolution at a slightly higher Reynolds number *Re*=8050 converges instead onto a periodic state with the frequency 0.44032 (see figure 7 (c)). The signal is no longer constant but oscillates in a periodic fashion as shown in the inset of figure 7 (c). This observation is indicative of the occurrence of a Hopf bifurcation for Reynolds number in between 8000 and 8050, as already well established in the literature [33, 39-41]. Beyond the Hopf point, infinitesimal perturbations are expected to grow exponentially thus rendering the steady state linearly unstable.

The critical Reynolds numbers separating periodic from quasi-periodic and quasi-periodic from chaotic flows have been studied in figure 8, by monitoring at the same point P_1 the time series of horizontal velocity u_x, phase-space trajectories of u_y vs u_x, and the Fourier spectrum of the velocity u_x. A systematic study across a wide range of Reynolds numbers covering the interval from 8000 to 20000 reveals that a second critical value arises for Reynolds numbers between 13500 and 14000. At *Re*=13500 the flow is still periodic while at *Re*=14000 the flow has become quasi-periodic. Chaotic dynamics appear at a Reynolds number between 16500 and 17000.

Figure 8 illustrates the different time-dynamics of the flow at the three time-dependent stages. Since the collection of critical values has been determined only approximately, the Reynolds numbers 8800, 14000 and 20000 have been chosen to represent the three different types of solutions, namely laminar unsteady periodic, laminar unsteady quasi-periodic and chaotic flows.

Figure 8 (a) shows a periodic solution at *Re*=8800, well beyond the Hopf bifurcation. A phase map projection on the (u_x , u_y) plane, shown in an inset, where u_x and u_y are the horizontal and vertical velocities at the probe in the center of the cavity (P_1), clearly illustrates the periodic nature of the solution as the trajectory exactly closes on itself. The main panel depicts the spectrum of the u_x signal in the upper inset. A sharp peak at $f = 0.4374$ accompanied by a series of harmonics, indicates that phase map trajectories wind with a period $T = 1/f = 2.2862$, which can be identified with the time period of the periodic solution.

Further increase in Reynolds number destabilizes the periodic solution into quasi-periodicity, as illustrated by the converged solution at *Re*=14000 shown in Figure 8 (b). The phase map projection clearly fails to close after a period and the loops keep drifting while winding on and densely filling an invariant two-torus. The spectrum retains the fundamental peak and harmonics of the periodic solution $f_1 = 0.66048$, but incorporates a second incommensurate frequency peak at $f_2 = 0.2944$ and the secondary peaks at all linear combinations of f_1 and f_2.

When the Reynolds number is increased further, the quasi-periodic solution is replaced by chaotic motion, as shown in Figure 8 (c) for *Re*=20000. The phase map projection winds haphazardly in the region of phase space where the quasi-periodic solution used to be, but a certain degree of deterministic chaos can be observed. As a matter of fact, while the spectrum still shows some indication of the original f_1 frequency, the fundamental peaks are now surrounded by broadband noise associated to chaotic dynamics.

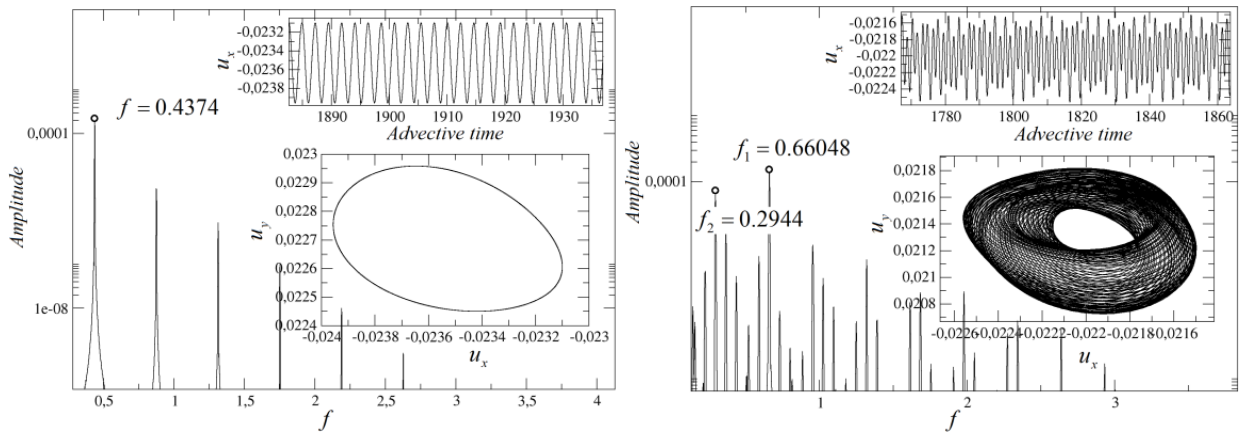

(a) Re=8800 (b) Re=14000

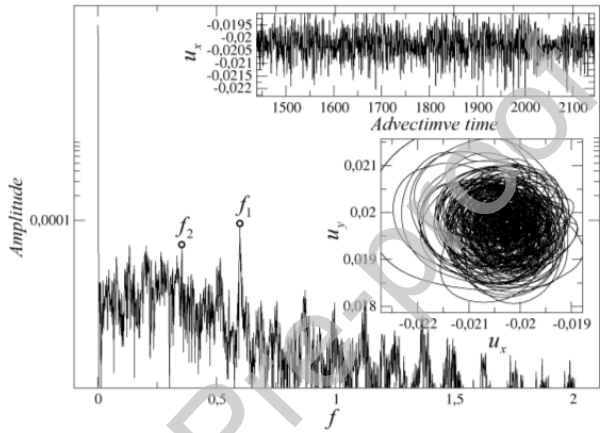

(c) Re=20000

Fig. 8. Time series of velocity u_x versus advective time, phase trajectory of u_y versus u_x and Fourier transform of time series u_x for case S1 at different Reynolds numbers. (a) Describes the periodic orbit at *Re*=8800. (b) Introduces the quasi-periodic solution at *Re*=14000. (c) Presents the chaotic solution at *Re*=20000.

To understand the energy associated to the different vortical structures, at a turbulent Reynolds number 20000, case *S1*, the spectral decomposition from the temporal velocity signal u_x obtained from the probe P_1, is presented in figure 9 (a). Notice that in the inertial subrange, the energy decays with a slope very close to -5/3, which proves that LBM with a grid resolution of 1024×1024, is capable of properly capturing the energy cascade. Nevertheless, the mesh is not dense enough to evaluate the dissipation range defined by the Kolmogorov scales. Figures 9 (b) and (c) present the streamlines topology and the vorticity contours for the same case and Reynolds number. When observing the spectrum, figure 9 (a), it can be seen two relevant frequency peaks, labelled as f_1 and f_2. Frequency f_1 is associated to the main vortex that occupies the centre of the cavity (see figure 9 (b)). The neat frequency peak at f_2 is instead related to the modulational dynamics of the smaller vortex located at the upper left corner. The collection of smaller peaks that appear at higher frequencies characterize the dynamics of the yet smaller vortices located at both bottom corners. The largest vortices have been shown to contain a higher level of energy, while the energy associated to smaller vortices decreases as their size decreases.

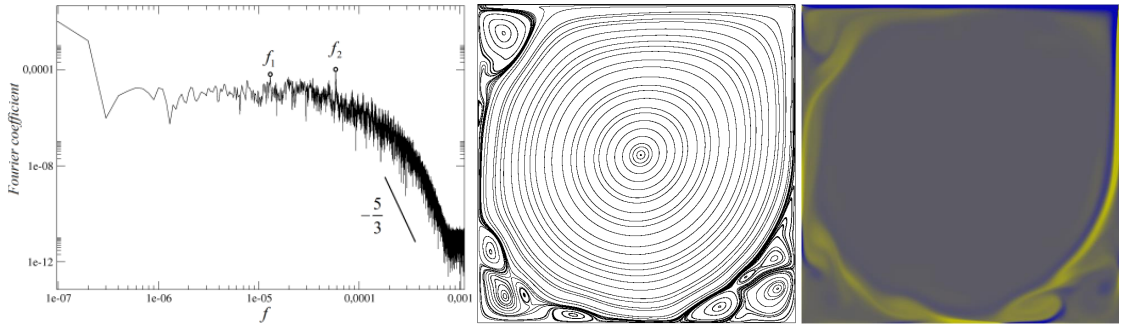

(a) (b) (c)

Fig. 9. (a) Spectral decomposition of time series u_x . (b) Introduces the streamlines at *Re*=20000. (c) Presents the vorticity contours at *Re*=20000.

Three videos, characterizing three different flow status, periodic, quasi-periodic and chaotic at Reynolds numbers 8800, 14000 and 20000 respectively, are presented as supplementary materials in the Appendix.

3.2. Transitional flow study for case S2p

For the case *S2p*, the same procedure as for the case *S2a* has been used. The main difference between cases *S1* and *S2p*, resides in that the information presented for case *S2p*, figures 10 and 11, were obtained using a probe P_3 located at $(x = L/2, y = 3L/4)$ (see figure 2 (a)). The Hopf bifurcation appears at a Reynolds number between 9500 and 9600 for the present configuration. The base steady state for the *S2p* cavity preserves the mirror symmetry (mirror reflection with respect to a horizontal line through the center of the cavity) as is clear from figure 10 (b), where the flow topology is again illustrated by streamlines. At *Re*=9500, two large counter-rotating vortices, slightly squeezed in the vertical direction, occupy the top and bottom hemispheres of the cavity. Each of the vortices has similar features to the core vortex of the *S1* case, except that they have been confined in shallower half cavities. Two smaller vortices, also mutually-symmetric appear on the stationary wall close to the corners from which the driving walls are moving away. The bottom stationary wall boundary of the *S1* cavity has now been replaced by a symmetry plane that acts as a slip wall. As a result, the upstream bottom vortex of case *S1* disappears while the downstream bottom corner persists, albeit largely modified, with no cascading of ever smaller vortices as happened for the *S1* case.

Figure 10 (a) displays the decay of a flow field perturbation onto the steady state at Reynolds number 9500. The time evolution of the horizontal and vertical perturbation velocity are represented in the top left panel. Notice that the signal asymptotically approaches a constant value. At *Re*=9600, the flow has become periodic instead with a frequency 1.4404, as shown in figure 10 (c). The instability has been pushed to higher Reynolds numbers as compared to the *S1* cavity as a result of the lower mean shear induced by two parallely moving walls as compared to a single moving wall with the opposing wall stationary. Although not shown in figure 10, the solution was found to be periodic at Reynolds number 9550 with frequency was 1.435.

Following the same methodology as for case *S1*, taking a large range of Reynolds numbers, numerical simulation reveals that the flow changes from periodic into quasi-periodic at a Reynolds number between 12250 and 13000. The critical value marking the appearance of chaotic flow is found to be between Reynolds numbers 16500 and 17000.

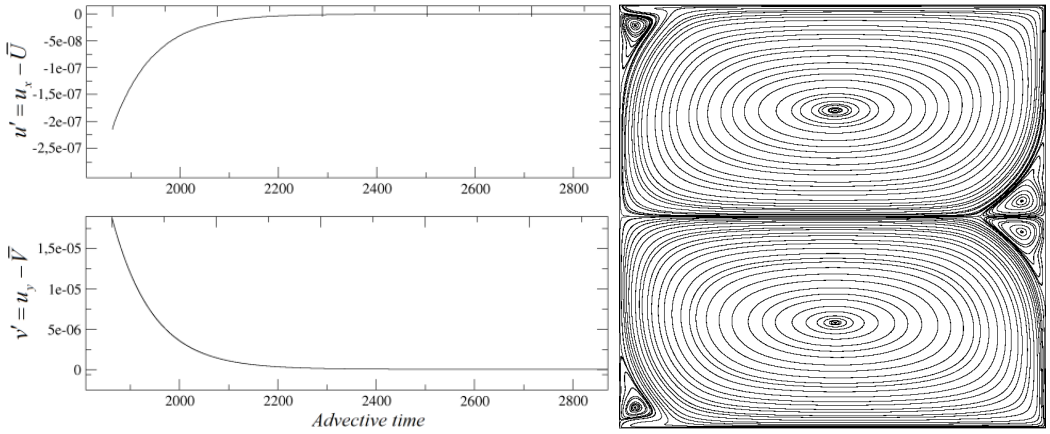

(a) (b)

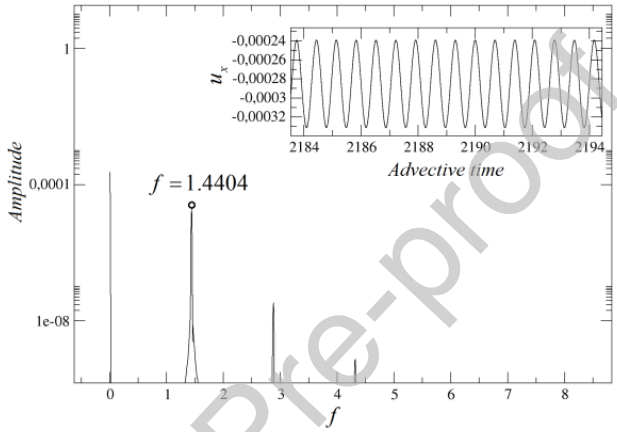

(c)

Fig. 10. (a) Perturbation of velocity history (u' and v') of the monitoring point at *Re*=9500. (b) Streamlines topology at *Re*=9500. (c) Periodic orbit at *Re*=9600.

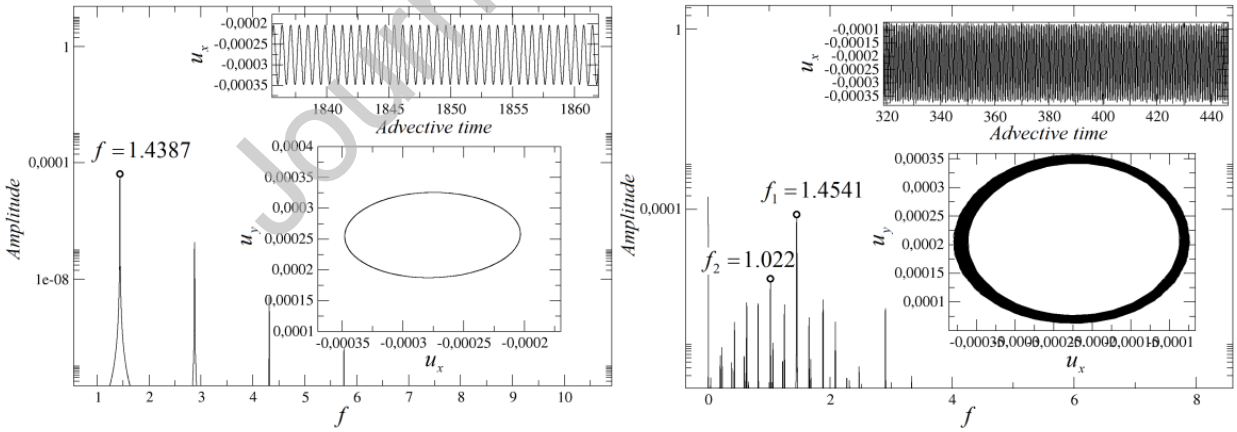

(a) Re=10000 (b) Re=14000

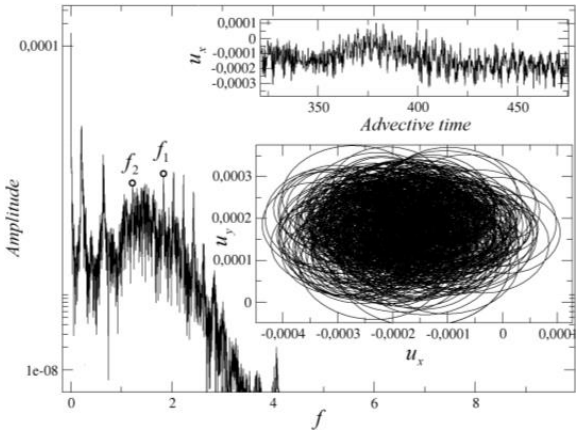

(c) Re=18000

Fig. 11. Time series of velocity u_x versus advective time, phase trajectory of u_y versus u_x and Fourier transform of time series u_x for case *S2p* at different Reynolds numbers. (a) Describes the periodic orbit at *Re*=10000. (b) Introduces the quasi-periodic solution at *Re*=14000. (c) Presents the chaotic solution at *Re*=18000.

Figure 11 presents the time series of velocity u_x, phase-space trajectories of the velocity u_x versus u_y, and the Fourier transform for three Reynolds numbers, 10000, 14000 and 18000, at which the flow is unsteady periodic, quasi-periodic and chaotic, respectively. At *Re*=10000, the phase map projection of figure 11 (a) shows that the solution is still periodic. As a matter of fact, the time signal seems to preserve a space-time symmetry, where evolving half a period is equivalent to a reflection with respect to the $y = L/2$ plane. The fundamental peak of the spectrum reveals that the frequency of the solution is $f = 1.4387$, which is of the same order of magnitude as that for the *S1* cavity but somewhat lower as a result of the smaller characteristic size of the vortices that are destabilized.

Figure 11 (b) shows how the space-time-symmetric stable periodic orbit has been replaced by a quasi-periodic solution at *Re*=14000. Quasi-periodicity enforces a final disruption of the symmetry which is no longer present except from a statistical point of view if sufficiently long time series are considered. The spectrum remains discrete but peaks arise at all linear combinations of the main $f_1 = 1.4541$ and secondary $f_2 = 1.022$ frequency peaks. At *Re*=18000 quasi-periodicity has already degenerated into plain chaotic dynamics. Trajectories evolve chaotically in phase space, yet in a structured fashion, and the spectrum has become continuous and broadband.

Figures 12 (a), (b) and (c) present the Fourier transform, the streamlines topology and the vorticity contours for case *S2p* at Reynolds number 18000 for the chaotic solution. Six relevant frequency peaks, defined as f_1 to f_6, and obtained from the probe P_3 are shown in figure 12 (a). The energy associated to the main vortex pair of figure 12 (b), has a frequency peak f_1 associated to it. The broad band covered by the peak is due to time modulation of the main vortex pair. This modulation is more clearly seen in the video presented in Appendix. The second peak, characterized by frequency f_2, is the second harmonic of the main frequency. The very neat peaks of frequency f_3 and f_4, are associated to the secondary vortices appearing at the central horizontal line and attached to the right hand side wall. These two vortices are very similar in shape, so that their frequencies are also very close. The peak at frequency f_5 corresponds to the two vortices appearing at left wall upper and lower corners. The tiny eddies appearing around the secondary and tertiary

vortices have associated frequencies around f_6. Notice that several peaks can be spotted around this particular frequency, characterizing the different dimensions of these tiny eddies.

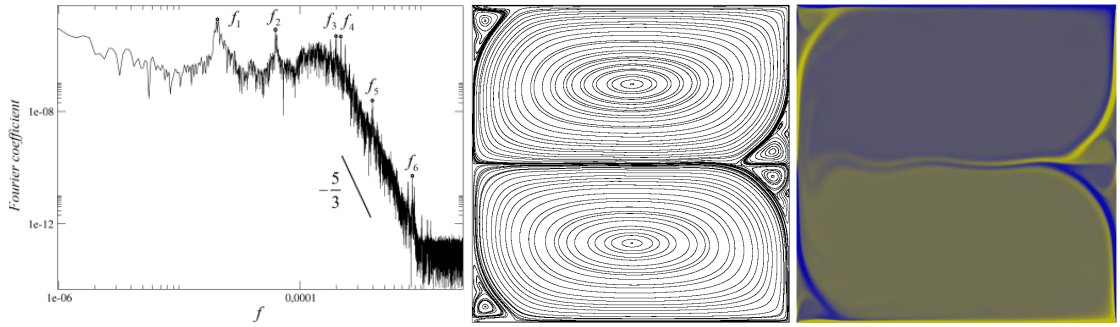

(a) (b) (c)

Fig. 12. (a) Spectral decomposition of time series u_x. (b) Introduces the streamlines at *Re*=18000. (c) Presents the vorticity contours at *Re*=18000.

Three videos, characterizing three different flow status, periodic, quasi-periodic and chaotic, at Reynolds numbers 10000, 14000 and 18000 respectively, are presented as supplementary material in Appendix.

3.3. Transitional flow study for case S2a

In order to investigate at which Reynolds number flow unsteadiness occurs, the probe P_3 located at $\left(x = L/2, y = 3L/4\right)$ (see figure 2 (a)), was employed. As already introduced in figures 7 (b) and 10 (b), figure 13 (b) characterizes for the present case, the streamlines topology at which the flow inside the cavity is steady.

Although the mean shear across a vertical line is double that of the regular *S1* cavity, the actual physics and location of the instability are such that the base steady state remains stable for Reynolds numbers all the way up to 10100, as shown in figure 13 (a). The flow topology (see figure 13 (b)), retains the core vortex and the left top secondary vortex of case *S1*, this latter now replicated at the bottom right corner. The steady state at *Re*=10100 clearly preserves the pi-rotation symmetry of the problem. At *Re*=10300, time series no longer converge unto a steady value but keep oscillating with frequency 1.2186, as illustrated in figure 13 (c). Although not shown, the flow is already periodic at *Re*=10200 with frequency $f = 1.2218$.

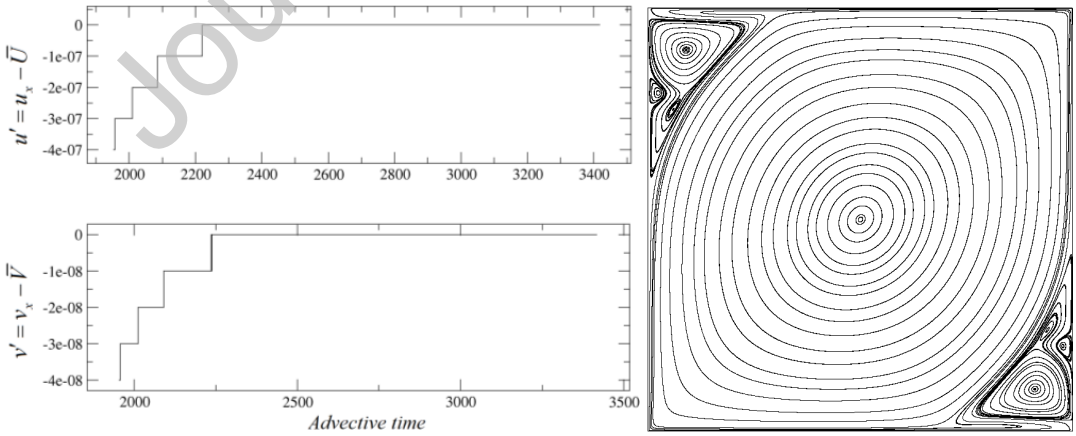

(a) (b)

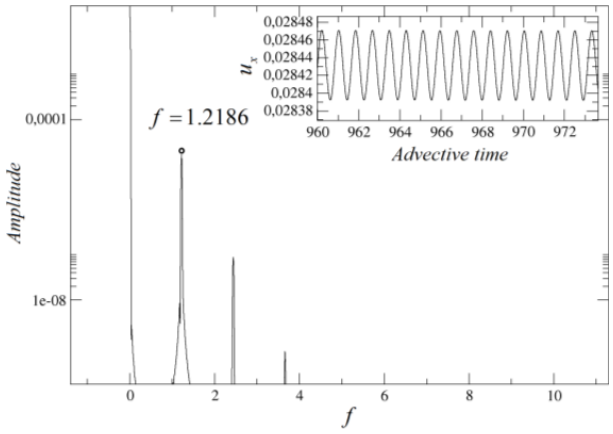

(c)

Fig. 13. (a) Perturbation of velocity history (u' and v') of the monitoring point at Re=10100. (b) Streamlines topology at Re=10100. (c) Periodic orbit at Re=10300.

Systematic simulation for Reynolds numbers beyond 10300 shows the occurrence of a Neimark-Sacker bifurcation. Quasi-periodic motion appears somewhere in between *Re*=11000 and *Re*=11100. The two frequencies associated to the quasi-periodic solution at *Re*=11100 are $f_1 = 1.2015$ and $f_2 = 0.13653$. Chaotic dynamics appear for Reynolds numbers between 17000 and 17500.

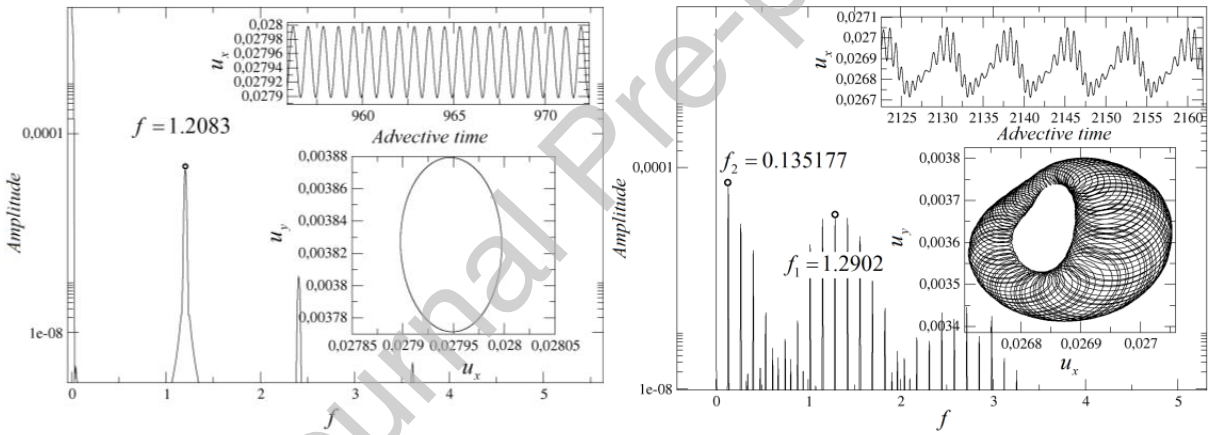

(a) Re=11000 (b) Re=14000

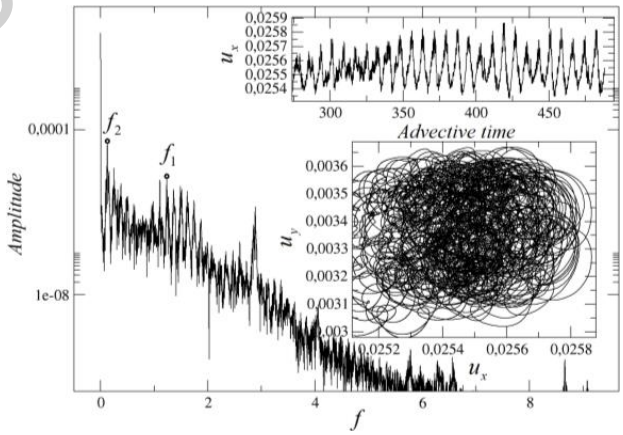

(c) Re=18000

Fig. 14. Time series of velocity u_x versus advective time, phase trajectory of u_y versus u_x and Fourier transform of time series u_x for case *S2a* at different Reynolds numbers. (a) Describes the periodic orbit at *Re*=11000. (b) Introduces the quasi-periodic solution at *Re*=14000. (c) Presents the chaotic solution at *Re*=18000.

The three different flow categories for case *S2a*, periodic, quasi-periodic and chaotic, are represented in figure 14, the following respective Reynolds numbers, 11000, 14000 and 18000 were chosen to characterize each category.

At *Re*=11000, the solution is periodic. The phase map and spectrum, see figure 14 (a), demonstrates the periodicity of the solution and allow to estimate its frequency as $f = 1.2083$. This frequency is roughly double that of the *S1* cavity $f = 0.6702$ at the same Reynolds number, such that it might indicate a different instability mechanism. At *Re*=14000, trajectories have become quasi-periodic as illustrated by phase map projections and spectrum of the velocity signal based on the readings of the probe P_3. A new modulational frequency $f_2 = 0.135177$ has appeared on top of the oscillatory frequency $f_1 = 1.2902$ inherited from the Hopf bifurcation.

Somewhere in between *Re*=16500 and 17000, the flow becomes chaotic. The phase map trajectory and the Fourier transform of the horizontal velocity signal at P_3 shown in figure 14 (c) clearly shows that the solution is highly chaotic at Reynolds number 18000.

Figures 15 (a), (b) and (c) show the spectrum, streamlines topology and vorticity contours, respectively, for case *S2a* at Reynolds number 18000. From the spectrum, three relevant frequency peaks, labelled as f_1, f_2 and f_3 can be observed. Frequency f_1, characterizes the highest energy level associated to the main central vortex in figure 15 (b). The clear peak at frequency f_2 is associated to the secondary vortices appearing at the upper-left and lower-right corners. Around this particular peak, several similar peaks also arise. We speculate that these peaks have the same origin at the two vortices at the upper-left and lower-right corners. As demonstrated by the video attached in Appendix, the secondary vortices are not temporally stable, which would account for the generation of time-dynamics at many different frequencies. The frequency f_3 is connected to the tertiary vortices appearing as well on the upper-left and lower-right corners.

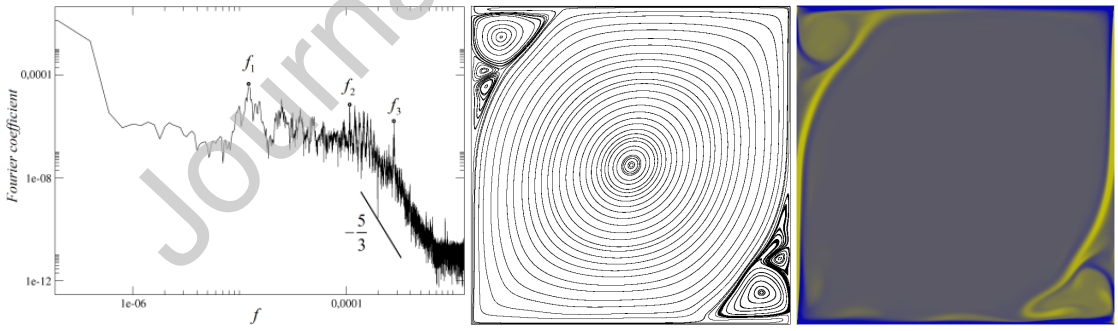

(a) (b) (c)

Fig. 15. (a) Spectral decomposition of time series u_x. (b) Introduces the streamlines at *Re*=18000. (c) Presents the vorticity contours at *Re*=18000.

Three videos, characterizing three different flow status, periodic, quasi-periodic and chaotic at Reynolds numbers 11000, 14000 and 18000 respectively, are presented as supplementary materials in Appendix.

3.4. Symmetry properties for two sided wall-driven cavities (cases S2p and S2a)

In the present subsection, and considering the driven conditions employed for cases *S2p* and *S2a*, the symmetry properties along with their critical Reynolds numbers will be investigated. In order to do so, for these two cases, two probes P_2 and P_3 were respectively located at positions $(x = L/2, y = L/4)$ and $(x = L/2, y = 3L/4)$. The time history of the velocity components u_x and u_y were recorded in each of these two probes. The norm of the difference between these velocities is chosen as the parameter to evaluate flow symmetry. Regarding the symmetry, for case *S2p*, the symmetry parameter employed to describe the mirror symmetry, is defined in equation (11), while for case *S2a*, the symmetry parameter defined in equation (12) is used to evaluate the pi-rotational symmetry.

$$\phi_A = \sqrt{(u_x^{L/2,L/4} - u_x^{L/2,3L/4})^2 + (u_y^{L/2,L/4} + u_y^{L/2,3L/4})^2} \tag{11}$$

$$\phi_B = \sqrt{(u_x^{L/2,L/4} + u_x^{L/2,3L/4})^2 + (u_y^{L/2,L/4} + u_y^{L/2,3L/4})^2} \tag{12}$$

This symmetry parameter is defined as a combination of the horizontal and vertical velocities measured on both probes. Notice that the difference between equations (11) and (12) resides on the sign associated to the velocity component u_x, measured in one of the probes. This modification is required since the u_x velocities on both probes have different directions in case *S2a*, they have the same direction for case *S2p*. It is found that the symmetry properties disappear at the following Reynolds numbers interval, (9500, 9550) and (10100, 10200) respectively for cases *S2p* and *S2a*. Figure 16 highlights this point.

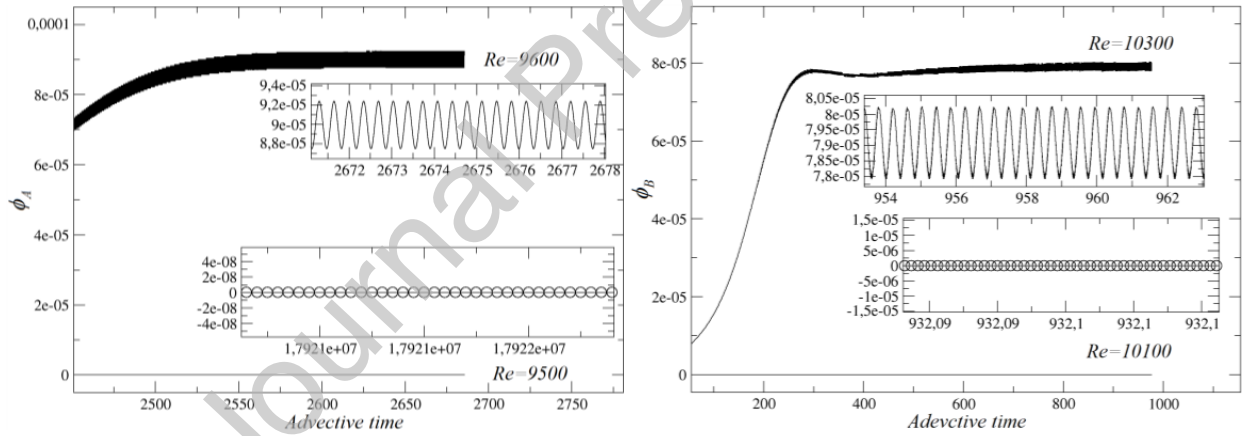

(a) Case S2p Re=9500 and 9600 (b) Case S2a Re=10100 and 10300

Fig. 16. Symmetric parameter versus iteration steps at different Reynolds for cases *S2p* and *S2a*.

Figure 16 shows the time evolution of the symmetry parameter for cases *S2p* and *S2a* at Reynolds numbers for which the symmetry has already been broken. The main panels (a) and (b) represent the symmetry parameter versus advective time. The insets zoom into the permanent regime. The Reynolds numbers shown correspond to the first symmetry-broken solutions, which happen to coincide with the first periodic solutions following the occurrence of the Hopf bifurcations. It is therefore highly probable that both Hopf points are symmetry-breaking bifurcations and that the onset of time-dynamics and the disruption of the symmetry occur all at once for both cases *S2p* and *S2a*. The frequency of the symmetry parameter is twice of the frequency

associated to the time series of u_x for both cases. This outcome is to be expected as the space symmetry disruption is in fact traded for a space-time symmetry whereby the evolution of the flow by half a period from any starting snapshot results in its exact symmetry conjugate. Although not presented in figure 16, the smallest Reynolds numbers at which symmetry no longer exist are found to be 9550 and 10200 for the cases *S2p* and *S2a*, respectively. The values of the symmetry parameters calculated are very small, ϕ_A is having a value around 1.5×10^{-10} and the value of ϕ_B is around 2.25×10^{-7}, indicating the onset of the asymmetry is around these Reynolds numbers.

Figure 17 shows the symmetric and symmetry-broken flow topologies for cases *S2p* and *S2a*. The symmetry-breaking is highlighted with a box containing the flow region in which the asymmetry is most clearly visible. For both cases, this happens in the vicinity of small scale eddy boundaries.

To better understand why the mirror symmetry disappears when the flow becomes periodic for case *S2p*, we have compared the symmetry-broken solution with the steady state at a slightly lower Reynolds number for which the solution is still symmetric. Close observation of the two small vortices located on the right hand side of the figure, right inside the box, shows that the upper one turns anti-clockwise, while the lower one turns clockwise. As a result, the flow on the central horizontal line separating the vortex pair is particularly unstable. Across this boundary, momentum interchange between particles is likely to occur. The turning speed associated to these small vortices is over five times bigger than the one associated to the main vortex pair. The line separating these small counter-rotating vortices is the location where the symmetry initially disappears.

An analogous analysis of figures 17 (c) and (d), which characterize the pi-rotational symmetric and asymmetric flow structure at Reynolds numbers 9000 and 11500, respectively, shows that the fluid along the curves separating the primary vortex and the secondary vortices located at opposite corners always flows in the same direction. The same occurs on the separation curves between the secondary vortices and tertiary vortices. A very thin elongated vortex, only visible in figure 17 (d) when zoomed in, is observed between the driving walls and the secondary vortices. These small elongated vortices prevent the fluid from flowing against the neighbouring moving lids. The area around these thin elongated vortices is particularly unstable, as the turning speed associated to these vortices is particularly high, such that here is where the pi-rotational symmetry initially disappears.

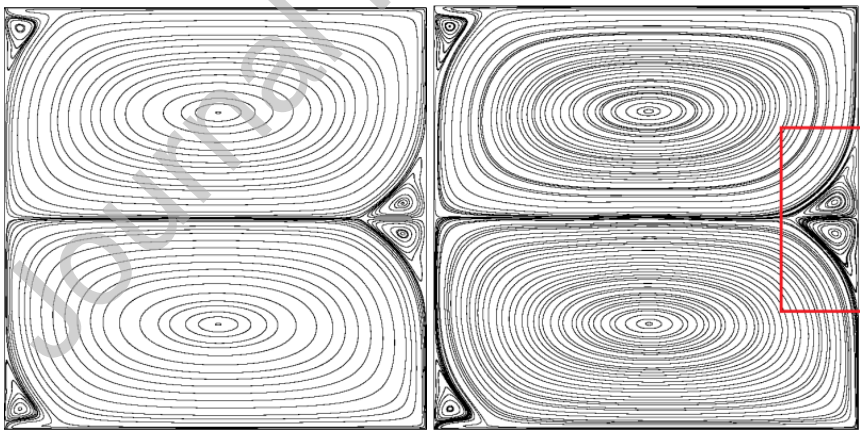

(a) Case S2p Re=9000 (b) Case S2p Re=9900

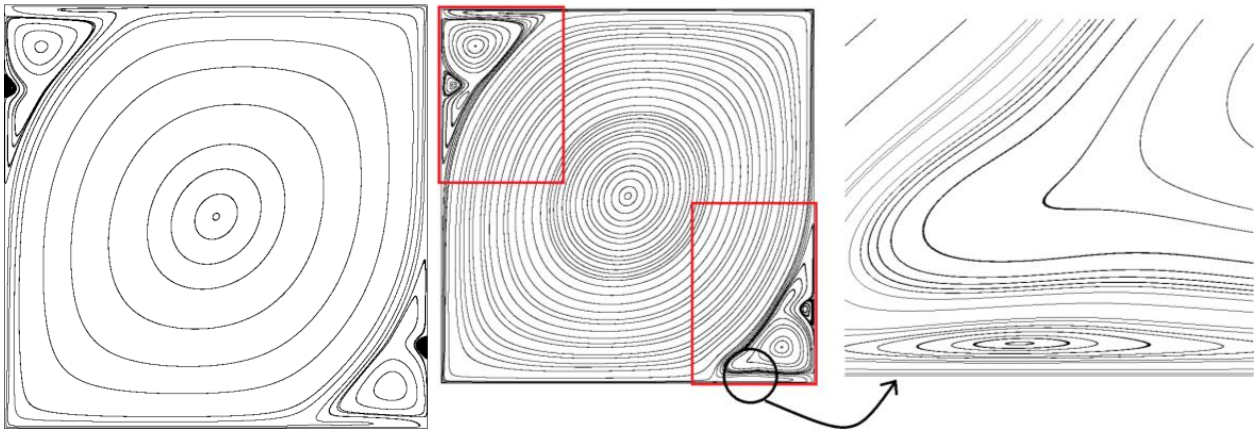

(c) Case S2a Re=9000 (d) Case S2a Re=11500

Fig. 17. Rotational symmetric and asymmetric structures of streamlines for cases *S2p* and *S2a* at different Reynolds numbers.

4. Conclusions

- For case *S1*, a Hopf bifurcation occurs at Reynolds number between 8000 and 8050, as already noted in the literature. By systematically analyzing a set of different Reynolds numbers, we determine that a Neimark-Sacker bifurcation occurs between Reynolds number 13500 and 14000.
- For cases *S2p* and *S2a*, the range of Reynolds numbers where the Hopf bifurcations occur are between 9500 and 9550, and between 10100 and 10200, respectively). The flow evolves from periodic to quasi-periodic at Neimark-Sacker bifurcations occurring in the Reynolds intervals 12250 to 13000 and 11000 to 11100, for the cases *S2p* and *S2a*, respectively.
- Regarding the onset of chaos, case *S1* produces a critical Reynolds separating it from quasi-periodic solutions between 16500 and 17000. The flow becomes chaotic between Reynolds number 16500 and 17000, for cases *S2p* and *S2a*.
- Symmetric properties have also been investigated for cases *S2p* and *S2a*. For case *S2p*, the mirror symmetry about the horizontal half plane disappears at the Reynolds number at which unsteadiness starts. For case *S2a*, a similar phenomenon is observed. The Reynolds number interval at which pi-rotational symmetry disappears, coincides also with the Hopf bifurcation.

Acknowledgements

The authors would like to acknowledge the financial support from the China Scholarship Council (CSC), from which the first author received a four-year scholarship to accomplish his PhD degree. This work was also supported by the Spanish and Catalan Governments under grants FIS2016-77849-R and 2017-SGR-00785, respectively.

Appendix

A total of 9 videos are provided in this paper. Three videos characterize case *S1* at Reynolds numbers 8800, 14000 and 20000, representing three stages (periodic, quasi-periodic and chaotic) of the flow. Three videos introduce the three different flow status (periodic, quasi-periodic and chaotic) for case *S2p* at Reynolds

numbers 10000, 14000 and 18000. The rest of the videos show transitional change among periodic, quasi-periodic and chaotic at Reynolds numbers 11000, 14000 and 18000 for case *S2a*.

References

[1] J.E. Broadwell, "Shock structure in a simple discrete velocity gas," The Physics of Fluids. 7, 1243-1247. (1964).
[2] U. Frisch, B. Hasslacher, and Y. Pomeau, "Lattice-gas automata for the Navier-Stokes equations," Phys. Rev. Lett. 56, 1505-1508 (1986).
[3] G.R. McNamara, and G. Zanetti, "Use of the Boltzmann equation to simulate lattice automata," Phys. Rev. Lett. 61, 20, 2332-2335. (1998)
[4] D.A. Wolf-Gladrow, "Lattice-gas Cellular Automata and Lattice Boltzmann Models: An Introduction," Springer, New York. (2000)
[5] S. Succi, "Lattice Boltzmann Equation for Fluid Dynamics and Beyond," Oxford: Clarendon Press. (2001)
[6] Y.L. He, Y. Wang, and Q. Li, "Lattice Boltzmann Method: Theory and Applications," Science Press, Beijing. (2008)
[7] Z.H. Chai and B.C. Shi, "A novel lattice Boltzmann model for the Poisson equation," Applied Mathematical Modelling. 32, 2050-2058 (2008).
[8] Y.L. Duan, and R.X. Liu, "Lattice Boltzmann model for two-dimensional unsteady burger's equation," Journal of Computational and Applied Mathematics. 206, 432-439 (2007).
[9] B.AN, and J.M. Bergadà, "A 8-neighbor model lattice Boltzmann method applied to mathematical-physical equations," Applied Mathematical Modelling. 43, 363-381 (2016).
[10] J.Y Zhang, G.W. Yan, and Y.F. Dong, "A new lattice Boltzmann model for the Laplace equation," Applied Mathematics and Computation. 215, 539-547 (2009).
[11] E.M. Viggen, "Acoustic multipole sources for the lattice Boltzmann method," Physical Review E, 87, 2, 023306, (2013).
[12] Y.A. Cai, J.H. Lu, and S. Li, "Direct simulation of acoustic scatter problems involving fluid-structure interaction using an efficient immersed boundary-lattice Boltzmann method," Journal of the Acoustical Society of America. 144, 4, 2256-2268 (2018).
[13] R.Z. Huang, and H.Y. Wu, "Total enthalpy-based lattice Boltzmann method with adaptive mesh refinement for solid-liquid phase change," Journal of Computational Physics. 315, 65-83 (2016).
[14] H. Amirshaghaghi, M.H. Rahimian, H. Safari, and M. Krafczyk, "Large eddy simulation of liquid sheet breakup using a two-phase lattice Boltzmann method," Computers & Fluids. 160, 93-107 (2018).
[15] S. Chen and C.G. Zheng, "Counterflow diffusion flame of hydrogen-enriched biogas under MILD oxy-fuel condition," International Journal of Hydrogen Energy, 36, 23, 15403-15413 (2011).
[16] S. Chen, Z.H. Liu, Z. He, C. Zhang, Z.W. Tian, and C.G. Zheng, "A new numerical approach for fire simulation," International Journal of Moden Physics C. 18, 2, 187-202 (2007).
[17] Y.H. Qian, D. d´Humières, and P. Lallemand, "Lattice BGK models for Navier-Stokes equation," Europhysics Letters. 17, 6, 479-484 (1992).
[18] C. Cheng, S.A. Galindo-Torres, X.B. Zhang, P. Zhang, A. Scheuemann, and L. Li, "An improved immersed moving boundary for the coupled discrete element lattice Boltzmann method," Computers & Fluids, (2018).
[19] U. Ghia, K.N. Ghia, C.T. Shin, "High-Re solutions for incompressible flow using the Navier-Stokes equations and a multigrid method," Journal of Computational Physics, 48, 3, 387-411. (1982)
[20] R. Schreiber, and H.B. Keller, "Driven cavity flows by efficient numerical techniques," J. Comput. Phys. 49, 310-333. (1983)
[21] S. Arun, and A. Satheesh, "Analysis of flow behavior in a two sided lid driven cavity using lattice Boltzmann technique," Alexandaria Engineering Journal. 54, 4, 795-806. (2015)

[22] L.A. Hegele, A. Scagliarini, M. Sbragaglia, K. Mattila, P.C. Philippi, D.F. Puleri, J. Gounley, and A. Randles, "High-Reynolds-number turbulent cavity flow using the lattice Boltzmann method," Physical Review E. 98, 4. (2018)
[23] D. Samantaray, and M.K. Das, "High Reynolds number incompressible turbulent flow inside a lid-driven cavity with multiple aspect ratios," Physics of Fluids. 30, 7. (2018)
[24] P.L. Bhatnagar, E.P. Gross, and M. Krook, "A model for collision processes in gases. I. Small amplitude processes in charged and neutral one-component systems," Physical Review, 94, 511-525. (1954)
[25] H.D. Chen, S.Y. Chen, and W.H. Matthaeus, "Recovery of the Navier-Stokes equations using a lattice-gas Boltzmann method," Physical Review, 45, R5339. (1991)
[26] A.J.C. Ladd, "Numerical simulations of particulate suspensions via a discretized Boltzmann equation. Part I. Theoretical foundation," J. Fluid Mech., 271, 285. (1994)
[27] Z.L. Guo, and C.G. Zheng, "Theory and Applications of Lattice Boltzmann Method," Science Press, Beijing, 2008.
[28] Z.L. Guo, C.G. Zheng, and B.C. Shi, "Non-equilibrium extrapolation method for velocity and boundary conditions in the lattice Boltzmann method," Chinese Physics, 11 (4):0366-0374. (2002)
[29] L.S. Lin, H.W. Chang, and C.A. Lin, "Multi relaxation time lattice Boltzmann simulations of transition in deep 2D lid driven cavity using GPU," Computers & Fluids. fluid Dynamics. 80, 381-387. (2013)
[30] C.H. Bruneau, and C. Jouron, "An efficient scheme for solving steady incompressible Navier-Stokes equations," Journal of Computational Physics. 89, 2, 389-413. (1990)
[31] A. Huser, and S. Biringen, "Calculation of two-dimensional shear-driven cavity flows at high Reynolds numbers," International Journal for Numerical Methods in Fluids. 14, 9, 1087-1109. (1992)
[32] A. Fortin, M. Jardak, J.J. Gervais, and R. Pierre, "Localization of Hopf bifurcations in fluid flow problems," International Journal for Numerical Methods in Fluids. 24, 11, 1185-1210. (1997)
[33] F. Auteri, N. Parolini, and L. Quartapelle, "Numerical Investigation on the Stability of Singular Driven Cavity Flow," Journal of Computational Physics. 183, 1, 1-25. (2002)
[34] Y.F. Peng, Y.H. Shiau, and R.R. Hwang, "Transition in a 2D lid-driven cavity flow," Computers & Fluids. 32, 3, 337-352. (2002)
[35] M. Sahin, and R.G. Owens, "A novel fully-implicit finite volume method applied to the lid-driven cavity problem Part I: High Reynolds number flow calculations," International Journal for Numerical Methods in Fluids. 42, 1, 57-77. (2003)
[36] C.H. Bruneau, and M. Saad, "The 2D lid-driven cavity problem revisited," Computers & Fluids. 35, 3, 326-348. (2006)
[37] A.K. Prasad, and J.R. Koseff, "Reynolds number and end-wall effects on a lid-driven cavity flow," Physics of Fluids A. fluid Dynamics. 1, 2, 208-218. (1989)
[38] C.S. Zhuo, C.W. Zhong, and J. Cao, "Filter-matrix lattice Boltzmann simulation of lid-driven deep-cavity flows, Part II – Flow bifurcation," Computers and Mathematics with Applications. 65, 1883-1893. (2013)
[39] V.B.L. Boppana, and J.S.B. Gajjar, "Global flow instability in a lid-driven cavity," International Journal for Numerical Methods in Fluids. 62, 827-853. (2010)
[40] J.C. Kalita, and B.B. Gogoi, "A biharmonic approach for the global stability analysis of 2D incompressible viscous flows," Applied Mathematical Modelling. 40, 6831-6849. (2016)
[41] A.N. Nuriev, A.G. Egorov and O.N. Zaitseva, "Bifurcation analysis of steady-state flows in the lid-driven cavity," Fluid Dynamics Research. 48, 061405. (2016)
[42] J.R. Koseff, and R.L. Street, "The Lid-Driven Cavity Flow: A Synthesis of Qualitative and Quantitative Observations," J. Fluids. Eng. 106, 4, 390-398. (1984)
[43] J.R. Koseff, and R.L. Street, "Visualization Studies of a Shear Driven Three-Dimensional Recirculating Flow," J. Fluids. Eng. 106, 1, 21-27. (1984)
[44] J.R. Murdock, J.C. Ickes, and S.L. Yang, "Transition Flow with an in compressible Lattice Boltzmann Method," Advances in Applied Mathematics and Mechanics. 9, 5, 1271-1288. (2017)